Scanning Near-Field Microwave Microscopy of VO_2 and Chemical Vapor Deposition Graphene

Alexander Tselev, Nickolay V. Lavrik, Andrei Kolmakov, and Sergei V. Kalinin*

Near-field scanning microwave microscopy (SMM) is a near-field technique, which enables probing local electric properties of materials, i.e., complex permittivity. Recently, this technique was incorporated into a commercially available atomic force microscope (AFM), providing a new powerful imaging mode in the suite of AFM techniques. AFM probe-surface distance control allows routine acquisition of near-field microwave images with a lateral resolution better than 100 nm, which was previously unattainable. In this paper, work performed with an AFM-based SMM system at the Center for Nanophase Materials Sciences at ORNL is reviewed. As an introduction, a brief general overview of the near-field microwave microscopy is provided followed by a description of the SMM system. Application of the technique to studies of metal-insulator phase transition in single-crystalline nanoplatelets of vanadium dioxide is illustrated. Further, the capabilities of SMM in its application to imaging of conductivity inhomogeneities in single- and few-layer graphene samples grown via different chemical vapor deposition (CVD) routes is demonstrated. The imaging of graphene illustrates the specific nature of contrast in the SMM, where the signal is described by complex numbers. To facilitate the interpretation of the contrast, a simple graphical scheme inspired by standard Nyquist plots is proposed.

1. Introduction

Analysis and control of inhomogeneities in materials is a key to understanding their properties and tailoring their performance in modern technology. Diversity of nanoscopic processes and desirable functionalities requires a broad variety of tools to access and characterize the local parameters of materials and nanoscale devices. In this regard, the most unique feature of the near-field scanning microwave microscopy (SMM) is that it enables direct non-invasive mapping of complex permittivity, which can be further used to locally access other related quantities such as, e.g., polarization in ferroelectrics or dopant distribution in semiconductors. Generally, SMM operates at frequencies from about 1 to 100 GHz. Electrical properties are not strongly frequency-dependent in this frequency range for majority of materials, and results of SMM can be applied to lower frequencies down to dc. Therefore, SMM is capable to provide access to the ground (as opposed to excited) state of materials, which is of the most relevance in many applications and studies of physical phenomena.

Comprehensive reviews of the SMM techniques were given by Rosner and van der Weide,[1] by Anlage, Talanov, and Schwarz,[2] and by Paulson and van der Weide.[3] Here we give only a brief overview of the field to introduce this subject to the broader audience. The term "near-field microwave microscopy" or alternatively "evanescent microwave microscopy" and "near-field microwave impedance microscopy", embraces a multitude of scanning probe techniques where electromagnetic waves in the microwave frequency range, i.e., from about 100 MHz to 100 GHz, are delivered to a sample and brought into interaction with it through an aperture, constriction, or a field concentrating feature such as a sharp tip with a size much smaller than the wavelength of the radiation both in air and in the sample (at a frequency f = 1 GHz, the wavelength of electromagnetic radiation in vacuum is λ = 30 cm). An aperture can be made in a wall of a resonant cavity or a waveguide, or it can be formed by the open end of a tapered transmission line. To a first approximation, the spatial resolution is determined by the size of the aperture or tip apex radius, not by the radiation wavelength, which allows one to overcome the diffraction limit of resolution in classical geometrical optics. An aperture or a field-concentrating feature should be scanned over the sample to obtain an image. In the case of aperture probes, the probe-sample interaction takes place through fields, which can be mathematically decomposed into a series of evanescent waves exponentially decaying away from the aperture at the length scale $\approx R_0$, the aperture size.

To overcome sensitivity limitations of aperture-based schemes, which necessarily operate below cutoff frequencies, Fee, Chu, and Hänsch[4] proposed, that a sharp tip terminating the central conductor of a coaxial transmission line or a signal contactor of a microstrip line can be used to increase the spatial resolution. Evanescent waves form around sharp tips as well.

Dr. A. Tselev, Dr. N. V. Lavrik, Dr. S. V. Kalinin
Center for Nanophase Materials Sciences
Oak Ridge National Laboratory,
Oak Ridge, TN 37831, USA
E-mail: tseleva@ornl.gov
Prof. A. Kolmakov
Physics Department
Southern Illinois University Carbondale
Carbondale, IL 62901, USA

DOI: 10.1002/adfm.201203435

However, to a first approximation, which is valid for the studies reviewed here, it is more convenient to look at such fields in a different way. In this approximation, the fringing (near) electric and magnetic fields and electric currents at distances $r < D << \lambda$, where D is the characteristic size of the probe-tip structure, can be treated as quasi-static, determined by the charge and electric current distributions in the proximate probe conductors at a given time moment, neglecting field retardation and derivatives of the fields over time (and hence, neglecting propagating waves and far-field radiation).[2] The fringing fields store reactive energy, and therefore the near-field probes behave like capacitors or inductors depending on predominant component of the electromagnetic field determined by probe configuration. The value of the probe capacitance or inductance is a function of the electric properties of a sample in the close vicinity of the probe, with higher sensitivity from regions with strongest fields. Therefore, measurement of the probe impedance with use of an appropriate model for the probe-sample system opens up a path to quantitative characterization of material local electrodynamics properties.[5–9]

During imaging, the impedance of the probe-sample system can be monitored by measuring the amplitude and phase of waves reflected directly from it through a transmission line.[4,10,11] To increase the system sensitivity and maximize the signal-to-noise ratio, a probe can be made as a load or a part of a resonator. Systems with coaxial resonators,[5] transmission line resonators of different types[7,8,12] and dielectric resonators[13,14] have been demonstrated. These systems take advantage of a strong frequency dependence of the resonator response in reflection or transmission. They either work at a fixed frequency close to the frequency of the largest slope of the response curve or follow and monitor the changes of the resonant frequency and Q factor of the resonator.

Since sharp tip probes currently provide highest resolution and sensitivity, they are used in the most of the modern SMM systems. Probes of this type behave like electric probes relying on capacitive coupling to the sample, with the probing field reactive energy being stored predominantly in the electric field. (Magnetic probes can be realized by shorting out the signal conductors of a coaxial or microstrip line to ground by a small wire loop;[6,12] the magnetic version of SMM is outside the scope of this paper.) Electric probes are sensitive to the sample dielectric function. Quantitative measurements of the material dielectric function is the most advanced among other applications of the SMM for quantitative characterization of materials.[15,16] In the past, near-field microwave imaging was also successfully applied for local sheet resistance measurements, and the technique was recently advanced to near-field imaging with nanometer and even atomic lateral resolution with a potential for quantitative material characterization at this length scale.[7,10–12,15,17–20] Simultaneous measurements of dielectric constant and conductivity (sheet resistance) can be accomplished by measuring the probe-sample response in a broad frequency range to properly take into account sample-dependent coupling between the probe and a sample.[21] Use of a broad frequency range in a resonator-less configuration was also proposed as a novel approach for elimination of parasitic contributions from microwave path imperfections and wave reflections from the probe surrounding.[22]

Alexander Tselev graduated with Master Degree in Radiophysics from Nizhniy Novgorod State University in Russia and received Ph.D. in Materials Sciences from Dresden University of Technology (TU Dresden) in 2000. He spent terms at University of Maryland, College Park, Georgetown University, and Duke University before joining the Center for Nanophase Materials Sciences at ORNL in 2009, where his research is primarily focused on near-field microwave microscopy and complex oxide thin films.

Nikolai V. Lavrik is a staff scientist at the CNMS, ORNL. He received his Ph.D. degree in physics from the Institute of Semiconductor Physics in Kiev and continued his work as a research fellow at the University of Illinois at Urbana-Champaign and University of Tennessee. Dr. Lavrik's research interests include fabrication and characterization of nanostructures with tailored optical, mechanical and mass transport functionalities. He has coauthored over 90 publications, including three book chapters, and received four R&D100 Awards.

Andrei Kolmakov graduated from Moscow Institute of Physics & Technology (MIPT) and received his PhD in solid state physics from Russian Research Center Kurchatov Institute in 1996. He was post-doctoral fellow at European Synchrotron Radiation centers ELETTRA/ HASYLAB, Texas A&M University, and University of California Santa Barbara. He joined the Department of Physics, Southern Illinois University at Carbondale in 2005 where he leads research on low dimensional materials.

The reliable imaging with a high spatial resolution requires bringing sharp probe tips in contact with or in a very close proximity to the sample surface. Therefore, the precise tip-sample distance control is a key component of any SMM system. STM-based distance control systems,[19,22,23] shear force-based

systems,[8,24] and cantilever-based probes incorporated in an AFM were used.[11,25–31] As was recently demonstrated, AFM-based SMM provides a great flexibility and highest spatial resolution, remaining, however, primarily a qualitative imaging, rather than quantitative characterization, technique.[18,20,32–35] Microscopes based on lumped element resonant circuits operating at microwave frequencies are also used. A prominent example of such a system is a non-linear dielectric microscope developed by Y. Cho.[36,37]

In the following sections, we will discuss the SMM system currently in use at the Center for Nanophase Materials Sciences (CNMS) at ORNL and illustrate its application to imaging of mesoscopic metal-insulator phase transition behavior in single-crystalline nanoplatelets of vanadium dioxide and to sub-100 nm mapping of conductivity inhomogeneities in graphene grown by chemical vapor deposition (CVD). The system is a result of recent advances in the technology, which enabled delivery of microwave energy to an AFM-style cantilever tip and use of the standard AFM tip-sample distance control. This combination provided SMM as one of the imaging modes available on a standard AFM platform. The very nature of the SMM signal, which is mathematically expressed in complex numbers, requires a specific approach to the image contrast interpretation. This will be illustrated with a simple graphical technique introduced for interpretation of contrast in images of CVD graphene.

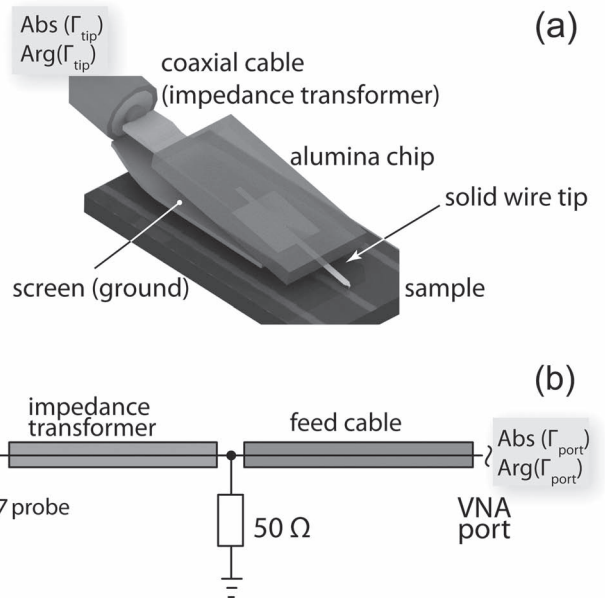

Figure 1. a) Schematic of the SMM probe with probe tip and sample. Abs(Γ_{tip}) and Arg(Γ_{tip}) are amplitude and phase of the reflection coefficient at the plane corresponding to the end of the coaxial geometry at the probe. b) Diagram of the SMM microwave path. Abs(Γ_{port}) and Arg(Γ_{port}) are amplitude and phase of the reflection coefficient at the port of the network analyzer. Abs(Γ_{port}) and Arg(Γ_{port}) are measured by the network analyzer and plotted to produce corresponding images. Reproduced with permission.[41] Copyright 2012, IOP Publishing Ltd.

2. Near-Field Microwave Microscope

The microwave path of the microscope available at ORNL's CNMS was designed and manufactured by Agilent Technologies, Inc. and is similar to that described in refs. [11] and [34]. The system can be used with both the Asylum Research MFP-3D and Cypher AFM platforms. **Figure 1**a illustrates the design and electrical configuration near the SMM cantilever. The cantilever (Rocky Mountain Nanotechnology) is made of a Pt solid wire and glued to an alumina chip fully compatible with standard silicon AFM tips. The Pt wire is etched to form a cone with an apex radius typically as small as 30 nm. The cone height is about 80 μm, which is noticeably larger than that for the standard Si tips—of about 30 μm. This relatively large height helps in reducing parasitic capacitance between a sample and the cantilever shank (horizontal part of the Pt wire). A clamp-style coupling electrically connects the cantilever shank with the central conductor of a coaxial cable. An important element of the design is the metallic platelet beneath the chip, which electrically shields the chip and the clamp from the sample. The shield is electrically connected to the outer conductor of the coaxial cable. Overall, the shield, clamp, and cantilever shank make up a configuration close to that of a microstrip line. The structure is affixed to a modified tip holder of the corresponding AFM platform in such a way that the same tip can be used in other imaging modes, such as ac (tapping) mode and c-AFM mode.

The detection system is made as a reflectometer measuring the amplitude and phase of the waves reflected from the probe and based on an Agilent vector network analyzer (Agilent E8364A). In the current embodiment, the probe is connected to a 50 Ω feed-cable running from a port of the vector network analyzer (VNA) through an impedance transformer terminated with a 50 Ω shunt resistor, as shown in Figure 1b. In this configuration, highest sensitivity is observed in narrow frequency ranges, where the impedance transformer becomes a $\lambda/2$ transformer. An exact $\lambda/2$ transformer converts a high impedance of the tip-sample system into itself; therefore in this case, the input impedance at the resistor is approximately 50 Ω. Since the 50 Ω resistor is a lossy element, the microwave energy at zero reflection (condition of a perfect match) is dissipated though the resistor rather than fully transferred to the probe, the network of the impedance transformer and the shunt resistor cannot be strictly called "matching" in respect to the impedance of the probe. However, the measurement sensitivity, especially in the phase channel, is higher with use of the transformer-shunt resistor circuit than in the case of direct measurement of the reflection from the probe.

The imaging is performed in the AFM contact mode. Information about local sample properties is contained in the amplitude Abs (Γ_{port}) and phase Arg (Γ_{port}) of the complex reflection coefficient Γ_{port} (S11 in scattering matrix terms) measured by the VNA at its port and plotted as corresponding—amplitude and phase— images simultaneously with images of sample topography.

3. Metal/Insulator Domains in Vanadium Dioxide

3.1. Variable-Temperature Imaging of Mesoscopic Heterophase Domain Formation

One of the research tasks where the SMM microscopy can be exceptionally efficient is imaging of domains of conducting (insulating) material in an insulating (conducting) matrix. In particular, SMM was very successfully employed to image nanometer-scale metal-insulating domains in a manganite thin films[18] and quantum Hall edge states in a two-dimensional electron gas.[38] Note, that in the cited works, the imaging was performed at cryogenic temperatures. In this regard, the use of microwaves for near-field imaging of low-energy excitations is the only choice due to the low energy of microwave photons. In fact, as was mentioned above, microwave imaging allows direct access to the ground state of a material (where use of an optical technique would result in high-energy excitations) and imaging directly of low-frequency conductivity and dielectric constant, which are generally close at dc and microwave frequencies (with possible exceptions in such cases as, for example, highly inhomogeneous materials with Maxwell-Wagner dielectric response or strongly disordered materials with hopping conduction).

These features of SMM imaging were recently used at ONRL's CNMS in the experiments on heterophase domain formation and studies of the phase transition behavior in the ferroelastic domain patterns in single-crystalline nanoplatelets of vanadium dioxide.[20] VO_2 is a strongly correlated electron material with a first-order metal-insulator phase transition (MIT) at a temperature of about 68 °C in the unconstrained bulk. At the transition, conductivity of the materials abruptly changes by several orders of magnitude, which is accompanied by a tetragonal-to-monoclinic structural transition. Due to the MIT, this material is of intense interest for numerous potential applications, especially in the form of thin films and nanowires. On the other hand, VO_2 is ferroelastic in the lower-symmetry semiconducting phase. Ferroelastic domain walls are symmetry-breaking interfaces within a homogenous material, where the deviations of the material behavior from the bulk due to symmetry change are controlled solely by the discontinuity of structural order parameters, as opposed to interfaces between dissimilar materials. Due to the large contrast in conductivity between low- and high-symmetry phases, VO_2 can be regarded as an ideal model system to explore the effects of symmetry breaking through studies of properties of ferroelastic domain walls.

The advantage of the SMM in this study stems from the fact that this technique does not require fabrication of electrodes connected to nanoplatelets owing to the capacitive coupling between the probe and sample. In fact, the mechanical stress induced by the deposited contacts makes the contacts inevitably invasive: contacts change fragile patters of ferroelastic domains in the low-temperature phase. Furthermore, the metallic domains ensconced in the insulating matrix will not be visible in any dc-current based conductive imaging mode.

Rectangular cross-section, high aspect ratio elongated single crystals (nanoplatelets) were used in the imaging experiments. The single-crystal nanoplatelets were grown by a vapor transport method along the surface of Si/SiO_2 substrates, and typically had a width in the range from 5 μm to 20 μm, thickness from a faction of micrometer to a few micrometers, and the length can be up to few hundred micrometers. As-grown nanoplatelets are firmly clamped to the substrate. The phase transition during cooling from the growth temperature induces mechanical strains due to crystal-substrate interactions. The overall elastic energy of the system is reduced by formation of ferroelastic domain structures in the nanoplatelets, and such structures were always present in substrate-clamped crystals.

The higher-symmetry metallic phase of VO_2, R, has a tetragonal, rutile, crystal structure (space group $P4_2/mnm$), whereas low-temperature and lower-symmetry semiconducting phase, M1, is monoclinic (space group $P2_1/c$). The monoclinic distortion of the tetragonal phase occurs as a shear deformation along the tetragonal *c*-axis so that the monoclinic two-fold axis b_{M1} is parallel to the tetragonal *a*-axis; the unit cell becomes doubled along the tetragonal *c*-axis. This structural transformation generates four pairs of antiphase domains. Four orientations of the domains correspond to four distinct directions of the monoclinic axis b_{M1} along $<100>_R$ directions of the parent lattice and can be visualized as consecutive rotations of one of the domains by 90° around the tetragonal *c*-axis. Regarding each pair of antiphase domains as one domain, we call pairs of orientational domains as 90° and 180° domains, according to the rotation angle within a pair. The M1-phase ferroelastic domains in the nanoplatelets can be readily observed using a polarized light optical microscope. Optical microscopy reveals two distinct patterns of the domains: labyrinth and parallel-plane. The domain walls in the labyrinth patterns are oriented along and perpendicular to the nanoplatelet length, i.e., the $[001]_R$ direction, while in the parallel-plane configurations, there are only domain walls perpendicular to the length. Detailed analysis further revealed that the labyrinth patterns consist of 90° domains, and the parallel-plane ones consist of 180° domains.[30] An important distinction between domain walls in these types of patterns is the size of the domain clapping angles associated with the domain walls, that is, the angles necessary to turn adjacent domain of the distorted structure to keep mechanical integrity of a crystal. Clapping angles between 90° domains are below 0.05°, which is a small value; whereas the clapping angles in the parallel-plane configuration are significantly larger, of about 0.23°. AFM topographic imaging of areas with parallel-plane domains reveals corrugated surface with parallel ridges and furrows running in the direction of the domain walls.[30] The labyrinth patterns do not produce any pronounced topographic features due to a small clapping angle associated with the 90° domain walls.

The set of SMM images showing development of metal and insulator domains over a labyrinth pattern on heating is displayed in **Figure 2**a. The images were taken at a frequency of about 1.8 GHz. The transition proceeds though formation and growth of metallic domains in the semiconducting matrix as is seen in the optical image in Figure 2b, taken at an intermediate state of the transition. An optical image of a labyrinth pattern in the insulating state is shown in Figure 1c. The elastic interaction with the substrate significantly broadens the metal-insulator transition over temperature. Each image in Figure 2a corresponds to a certain temperature in the MIT range and was obtained by overlaying microwave signal over simultaneously

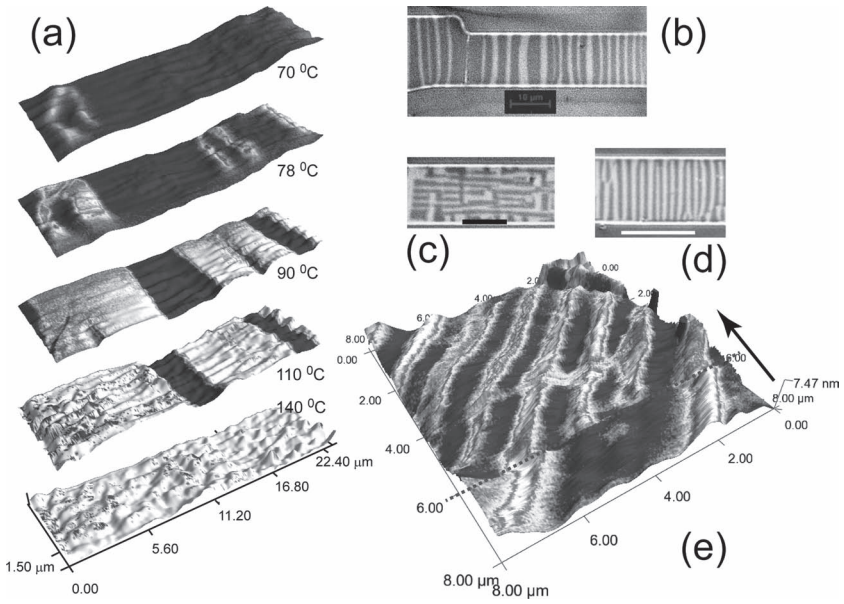

Figure 2. Near-field microwave imaging of metal-insulator domains in VO_2 nanoplatelets. a–c) Development of metallic domains on heating in a nanoplatelet portion with labyrinth ferroelastic domain pattern in the insulating state. a) The SMM signal is overlaid over topography image; b) optical image of metallic (dark) and insulating (bright) domains at an intermediate stage of the transition; c) polarized light optical image of a labyrinth pattern of ferroelastic domains in the insulating phase. a–c) show the same portion of a nanoplatelet. d) Polarized light optical image of a parallel-plane pattern of ferroelastic domains. e) Development of metallic domains over the parallel-plane ferroelastic domain structure. The SMM signal is overlaid over topography. The arrow shows direction of scan. The temperature was raised by 2 °C during the scan at the moment corresponding to the dashed line. Scale bars in b), c), and d) are 10 µm. Adapted with permission.[20,30] Copyright 2010, American Chemical Society.

acquired topography. White color corresponds to the metallic phase, while black shows the semiconducting phase. As seen in Figure 2a, the metallic domain formation starts upon heating with irregularly shaped domains elongated across the nanoplatelet. They grow into wider stripes spanning the whole nanoplatelets width so that domain boundaries turn perpendicular to nanoplatelet sides. This orientation of heterophase domain wall reduces the elastic energy of the system. Due to a larger lattice constant of the metallic phase along the normal to the surface, there are steps in the nanoplatelet thickness at the heterophase domain boundaries clearly visible in topography. Upon further heating, metallic domains grow at the cost of the semiconducting phase by the motion of domain walls. It was observed, that domains may re-arrange so that some areas, where transition to the metal phase had already occurred, become again semiconducting. This locally re-entrant phase transition behavior clearly illustrates the role of long-range elastic interactions and mobile boundary conditions on the MIT transition dynamics.

The picture of the MIT over the areas with parallel-plane configuration of ferroelastic domains looks distinctly different. Figure 2e displays a topographic AFM image with simultaneously acquired SMM signal overlaid over topography at an intermediate state of the MIT in a structure of parallel-plane domains (an optical image of the structure is shown in Figure 2d). The direction of the slow scan is indicated with an arrow in the figure. At the scan line marked by the dashed line, temperature was increased by about 2 °C, and number of new metallic domain appeared. Note that metallic domains nucleate at the ridges, elongate along them, and broaden into furrows of the corrugated topographic structure. The ridges with metallic domains look slightly elevated above the surface. This is due to expansion of the lattice as a result of the structural transition. After transition is complete, the surface becomes randomly rough, and on cooling, the structure re-appears in reverse order so that metallic domain disappear in the ridges. The imaging revealed that the opening of conductive channels at ferroelastic 180° domain walls takes place at temperatures well below the bulk transition temperature (about 12 °C).

Structurally, an 180° domain wall corresponds to a lost mirror plane of the higher-symmetry rutile lattice. This means an effective raise of the local symmetry at the wall plane. Atomic arrangement, interatomic bond lengths and angles in the wall vicinity may resemble those of the parent structure, which should lead to local decrease of the phase-transition-driving order parameter and appearance of the higher-symmetry phase properties at temperatures well below the bulk phase transition, as observed in the SMM experiments. In support of this argument, ab initio calculation of the electron spectrum showed band gap closure at a distance of about one unit cell from an unconstrained 180° domain walls suggesting significant lowering of the local energy barrier for nucleation of the metallic phase along the walls of this type.[20] However, generally in addition to the intrinsic symmetry breaking mechanisms, the behavior in ferroic domain walls can be driven by extrinsic factors related to the long-range electrostatic, chemical, or strain fields. In the particular case of the 180° domain walls, the separation of the domain walls by properties in the phase transition is apparently stress-driven. Namely, at low temperatures, the material is more under compression at the ridges than at furrows, and this extra compression promotes the observed nucleation of metallic domains at ridges. At the same time, the imaging experiments over the labyrinth patterns indicated that 90° domain walls do not serve as preferential sites for nucleation of the metallic phase and do not show a distinct behavior in the phase transition. This can be explained using simple considerations based on Ginzburg-Landau phase transition theory and the analysis of the change of the structural order parameter across a wall.[30,39]

On the instrumental side, it is of interest to note that the SMM imaging resolution in these experiments was determined by the radius of the probe tip and therefore, is approximately equal to the resolution in respect to topography, i.e., ≈20 nm in our case. However, the SMM resolution is significantly limited by the sensitivity of the microwave electronics. In the detection configuration used, the minimal detectable area of a metallic patch imbedded into semiconducting matrix was ≈0.12 µm^2.

3.2. Electromechanical Actuation in Suspended VO_2 Nanoplatelets

Continuing the theoretical and experimental effort on investigation of heterophase domain formation in nanoplatelets initiated with use of SMM, in the next work, we addressed behavior of heterophase domain structures in free-standing, suspending nanoplatelets in the presence of electrical current. It was found that the stress-controlled formation of metal-insulator domain structures, which stems from the coupling of electronic and structural aspects of the MIT, can be employed to generate electrically controlled mechanical motion and to achieve actuator action at the nanometer scale. A novel concept of generation of the mechanical motion was proposed in ref. [40]. In suspended nanoplatelets, sufficiently strong electrical current and resulting Joule heating lead to formation of metastable heterophase domain patterns where domains are arranged in such a way that there exists a continuous path for the current flow through a chain of metallic domains. The mixed metastable state is sustained by the inhomogeneous temperature and strain distributions. This coexistence state results in nanoplatelet bending due to the difference in the lattice parameters of metallic and semiconducting phase. The bending depends on the current strength. **Figure 3**a shows a current-carrying nanoplatelet suspended between liquid-metal electrodes in the mixed state with triangular and trapezoid domains resulting in nanoplatelet bending. In these experiments, the substrate of the device was used as a heater. The substrate temperature in Figure 3a was 44 °C. Figure 3b shows the same nanoplatelet in an experiment demonstrating generation of mechanical motion. The nanoplatelet was preheated above the transition temperature, and then a current of about 0.7 mA was sent through it. After cooling down to a substrate temperature of about 64 °C, a domain of semiconducting phase appeared at the growth defect at the edge of the nanoplatelet as is seen in Figure 3b, and the nanoplatelet bent both at the domain site and in the vicinity of the contacts. After current increase to 1.8 mA, the semiconducting domain disappeared, and the nanoplatelet straightened. Stepping the current between 0.7 and 1.8 mA, the nanoplatelet could be repeatedly changed in shape from straight to bent and back. Furthermore, it was shown that by increasing current through the nanoplatelet, the substrate temperature can be lowered down to room temperature while keeping the nanoplatelet in the metallic state; however, a stable and repeatable nanoplatelet deformation could not be realized in this regime with this particular species. It could be done, however, with somewhat thicker and wider crystals, which indicated that the actuation action can be realized over a wide temperature range, including substrates at room temperature. Analyzes performed in the work showed, that if this phenomenon were used for electrically controlled motion generation, achievable displacements are comparable to those characteristic for existing electrothermal actuator designs, while operational temperatures can be dramatically smaller.

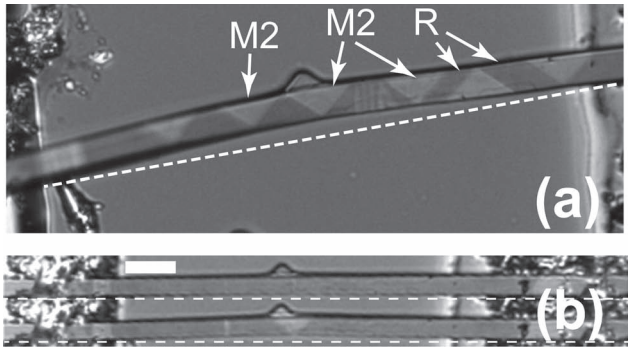

Figure 3. Electromechanical actuation in suspended VO_2 nanoplatelets. a) Optical images of a VO_2 nanoplatelet carrying a current of ≈2 mA at a substrate temperature 44 °C; the nanoplatelet is in the mixed state. The nanoplatelet length between electrodes is 180 μm, and its width is 8 μm. b) Cycling of the nanoplatelet between straight and bent states by stepping the current through it from 1.8 to 0.7 mA and back; substrate temperature is 64 °C. "M2" and "R" denote insulating M2 and metallic R phases of VO_2 as were identified by X-ray microdiffraction. Scale bar in (b) is 20 μm. Adapted with permission.[40] Copyright 2011, American Chemical Society.

4. Imaging of CVD Graphene

4.1. Conductivity Inhomogeneities in CVD Graphene

As we saw in the case of imaging domains in VO_2, the response of the SMM microscope is determined by the size of the metallic domain and its capacitance in respect to the conducting substrate. In the case of an insulating substrate, the response will be determined by the metallic domain capacitance with respect to the system ground. If our goal is to distinguish between metallic and insulating phases without necessity to go into details of how conductivity is distributed within a highly conducting domain, the measurement configuration described thus far is sufficient. However, it does not allow resolving inhomogeneities within conducting domains, since the response is determined by the domain as a whole (with a possible contribution from contact resistance between the probe tip and domain). It makes it clear that microwave imaging of inhomogeneities in large samples of highly conducting materials impose a specific challenge since meaningful imaging with a direct electrical contact between tip and the sample is problematic. In fact, the image contrast in the case of a direct tip-conducting sample contact is dominated by the tip-sample contact resistance, similar to conductive AFM. In this case, the measurement system requires a large dynamic range to be able to track large changes in contact resistance and in conducting domain sizes. Moreover, highly possible contact bounce with sporadic and abrupt changes of the contact resistance further complicates both imaging and data interpretation. To resolve these problems, reliable and yet sufficiently strong capacitive coupling between the probe and sample is required. Obviously, imaging quality will crucially depend on the way how this coupling is realized.

This issue can be further illustrated by results of ref. [32]. The authors imaged isolated graphene islands in a SiO_2/p^{++}-Si substrate, and the coupling between the probe tip and graphene took place through the direct tip/graphene electrical contact with imaging frequency of about 1 GHz and a tip-based Pt.

The electrical circuit was complete through a relatively large capacitance between the graphene islands and the underlying conducting substrate. Inhomogeneities within the islands were imaged with a ≈100 nm lateral resolution. It was possible to distinguish and assign sheet resistance values to flakes of graphene produced with different methods. Analysis of the images supported by numerical simulations clearly showed that the image contrast originated from the three factors: (1) local graphene sheet resistance, (2) variations of the contact resistance and contact capacitance, (3) overall capacitance of the islands in respect to the underlying conducting substrate with the last factor being the dominant one. Consequently, graphene islands of only limited size—of a few μm—could be imaged. In turn, Talanov et al.[9] implemented a parallel-plane strip-line resonator probe at about 4.5 GHz imaging frequency with shear-force probe-sample distance control system. Such probes are electrically balanced, i.e., signal and ground electrodes are indistinguishable, which significantly simplifies quantitative measurements of electrical properties. This approach allows purely capacitive coupling between the probe and graphene. However, with use of relatively blunt balanced probes, the spatial resolution of this technique is approximately 1 μm, which is much lower than that achievable with unbalanced, tip-based probes.

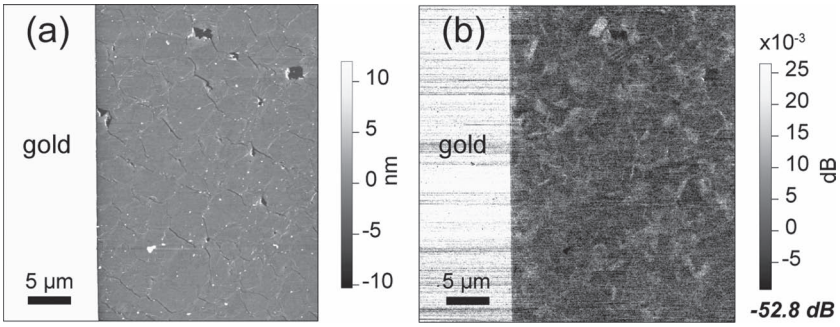

Figure 4. a) Topographic and b) amplitude SMM images of a of a large-area few-layer graphene sample grown on a Ni film at a reduced temperature using acetylene as a carbon source. The SMM image was acquired at 1.8 GHz. "gold" marks a 50-nm-thick gold stripe lithographically defined on top of graphene. The greyscale bar in (b) shows the change of the signal in respect to the value shown under the scale bar. Scan size is 35 μm × 35 μm. Reproduced with permission.[41] Copyright 2012, IOP Publishing Ltd.

In our subsequent work on SMM imaging,[41] we implemented deposition of a thin insulating layer on top of large-area graphene films to investigate conductance inhomogeneities in the films. A reliable capacitive coupling between the probe tip and graphene was achieved by depositing a 4-nm-thick layer of Al_2O_3 over the whole sample using atomic layer deposition (ALD). ALD process results in topography-conformal films with uniform thickness over large areas as required for the constancy of the capacitive coupling between the tip and the sample.

To test the effect of the insulting layer on the dynamic range of the microscope, a few-layer graphene film was imaged in one frame together with a metal film. Growth of the few-layer graphene was intentionally performed at a relatively low temperature with a chemical vapor deposition (CVD) process on a Ni catalyst film, which resulted in "grainy", inhomogeneous graphene reflecting the grainy structure of the catalyst film. After growth, the graphene film was transferred on a SiO_2/Si substrate, and a pattern of 30-μm-wide and 20-nm-thick parallel gold stripes was defined on the surface using a photolithographic process. This allowed us to have a spectrum of sheet resistances spanning from near zero for the gold stripes to infinity for open areas of the substrate within one scan frame. The alumina layer was deposited over the whole sample surface right before the SMM imaging. **Figure 4** displays topographic and SMM images (amplitude channel) of this sample. The SMM image was acquired at a frequency of about 1.8 GHz. One of the gold stripes appears on the left in the images. The details in graphene on the right side of the SMM image are well-resolved. The signal over the gold stripe is not saturated. This demonstrates that deposition of a thin insulating layer results in a sufficiently large dynamic range to image details in the relatively highly resistive graphene together with highly conducting gold in one scan frame. The SMM image clearly shows grains of varying conductivity in the graphene film with substructures at a smaller length scale, which are not visible in the topographic image. Imaging of a variety of inhomogeneous few-layer graphene films allowed determination of a spatial resolution of the technique in this imaging approach. The lateral resolution was found to be ≈50 nm, which is approximately the radius of the probe tip apex.[41]

Figure 5 shows a set of images of an isolated conducting object—a single-layer graphene island of about 10 μm in size. Such islands were grown on Cu foils using a CVD process. After growth, the islands were transferred onto a SiO_2/Si substrate for imaging. The thickness of graphene layers in identically grown sample was verified by a number of direct and indirect methods: high-resolution transmission electron microscopy (HRTEM), low-energy electron microscopy (LEEM), low-energy electron reflectivity in correlation with Raman spectroscopy and scanning electron microscopy (SEM). Based on the results of the comprehensive studies, micro-Raman spectroscopy was used to determine the number of layers in this particular sample. Figure 5a–c display topographic, SMM

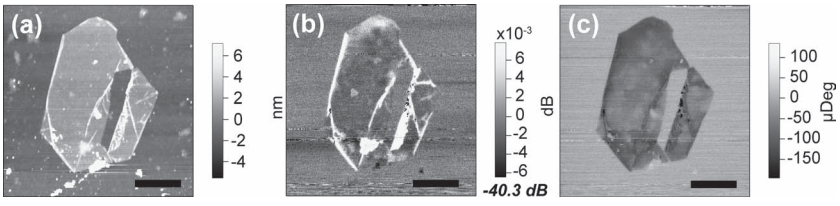

Figure 5. a) Topographic, b) amplitude, and c) phase SMM images of an isolated single-layer graphene island grown on a 25-μm-thick Cu foil. The SMM images were acquired at 5.2 GHz. The greyscale bars in (b) shows the change of the signal in respect to the values shown under the bars. Scan size is 20 μm × 20 μm. Scale bar is 5 μm. Reproduced with permission.[41] Copyright 2012, IOP Publishing Ltd.

amplitude, and SMM phase images, respectively. The SMM images were obtained at a frequency of 5.2 GHz. The bright areas in the amplitude image correspond to lower sheet resistance in areas, where there is more graphene material: wrinkles, folds, and curled edges. SMM images reveal sub-micrometer scale inhomogeneities across the graphene islands, which can be attributed to contamination of graphene by light residues of PMMA resist used in the substrate transfer process. It has to be noted that the ALD process required remote plasma activation to obtain a smooth alumina film of graphene surface. The plasma activation inevitably introduces some degree of damage in the graphene films, which in turn, increases graphene sheet resistance. However, graphene portions protected from the ALD plasma by thicker residues of PMMA remain highly conducting, and this is clearly visible as a bright spot in the amplitude image in the lower part of the island, even though the residue reduces the capacitive coupling between graphene and the probe tip. In turn, the main effect of the light PMMA residues is a variable degree of protection from the ALD plasma, with the plasma damage being reflected in the varying graphene sheet resistance. Variations of the residues thickness are also reflected in the observed contrast.

There is, however, an apparent difficulty in interpretation of the details of the SMM contrast when the amplitude and phase images are compared. Note that in the amplitude and phase SMM images, the contrast has different sense versus sheet resistance with a noticeably smaller intensity across the island in the phase image. Further, in the amplitude image, graphene bulk is almost indistinguishable from the non-conducting substrate, while in the phase images, the island is clearly seen against the substrate. To interpret the images, a detailed analysis of the contrast formation mechanism was required, and it was performed as outlined below (see more details in ref. [41]). The analysis has a general importance for microwave imaging in the resonator-less reflectometer configuration.

4.2. Contrast Mechanism in Microwave Images of Graphene

To understand the image formation, we consider the tip sample system in so-called quasi-static approximation, which is valid, when a microwave frequency is low enough so that the characteristic probe-sample system size $L \ll \lambda$, where λ is the wavelength of the electromagnetic radiation in the media surrounding the probe. With imaging frequencies below $f = 6$ GHz, $\lambda > 5$ cm in air, and at a characteristic probe size of about 1 mm, the quasi-static approximation can be sufficient. Graphene is a two-dimensional conductor, which makes it a good, simple system for the image formation analysis since microwave current is confined in the graphene film. In the quasi-static approximation, a graphene film on a SiO_2/Si substrate is a distributed system, which can be modeled by a network of capacitors and resistors as illustrated in **Figure 6**. The amplitude and phase of the reflection coefficient are determined by the impedance of the whole system consisting of both a sample and the probe. However, due to a strong enhancement of the electric field by the sharp probe tip, relative contribution of the material in the immediate vicinity of the tip apex dominates in the change of the impedance of the probe-sample system, which results in appearance of the image contrast. The contributions of fields and currents away from the tip apex are averaged out and result in gradual, non-localized, changes of the signal across an image. Consequently, the main contributions in the impedance are from the distributed film-substrate capacitance through the substrate oxide layer, spreading resistance of the film, and the tip-film coupling capacitance through insulating layer at the tip. Therefore, for an approximate analysis, a simplified lumped-element model shown in **Figure 7**a can be considered. The model consists of only four elements: tip-sample coupling capacitance C_{coupl}, graphene spreading resistance R_s, capacitance of the SiO_2 layer C_{ox}, and the parasitic stray capacitance between the tip cone and the microwave ground C_{str}. Figure 7a also explicitly shows the capacitance C'_{coupl} between the sample and the ground. Obviously, $C'_{coupl} >> C_{coupl}$ is required for successful imaging.

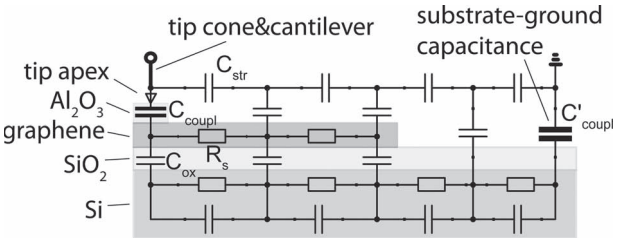

Figure 6. A quasi-static lumped element model of the SMM probe sample-system stressing its distributed nature. Reproduced with permission.[41] Copyright 2012, IOP Publishing Ltd.

For further analysis, we use a technique, which we may call "R_s-plot" technique.[41] An R_s-plot is a plot of the complex admittance Y_{tip} of the tip-sample system at a given angular frequency

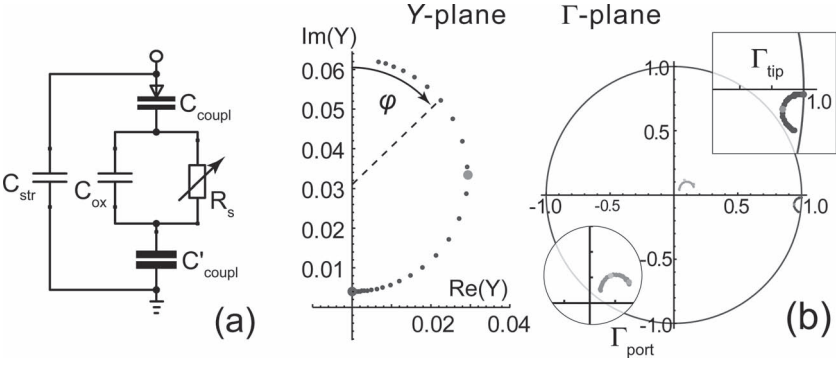

Figure 7. a) A simplified lumped-element model of the probe-sample system shown in Figure 6. b) Left panel shows a generic Y-plane R_s-plot for the circuit in (a) in the case $C_{str} = 0$ and $C_{coupl} >> C_{ox}$. The plot is made with logarithmically spaced R_s-values. The right panel shows images of this plot in the Γ-plane for the two cases: (i) at the reflection plane at the probe sample system, Γ_{tip} (close to the point $\Gamma = 1$), and (ii) at the VNA port, Γ_{port} (close to the Γ-plane origin). The orientation of the semicircle in the Γ-plane is arbitrary for uncalibrated measurements. Larger and brighter dots in the plots correspond to maximal Re(Y) and to R_s equal to infinity. Reproduced with permission.[41] Copyright 2012, IOP Publishing Ltd.

ω in Cartesian coordinates (Re(Y), Im(Y)) with use of R_s as a plot parameter. A generic R_s-plot for the simplified circuit in Figure 7a with $C_{str} = 0$ and $C_{coupl} >> C_{ox}$ (C'_{coupl} is absorbed by C_{coupl}) is shown in the left panel of Figure 7b. Note, that this is a perfect semicircle with the center on the imaginary axis. The radius of the semicircles is

$$s = \frac{1/2\omega C_{coupl}}{1+C_{ox}/C_{coupl}},$$

and it passes through points with coordinates $(0,\omega C_{coupl})$ at $R_s = 0$ and $(0,\omega C_{coupl}C_{ox}/(\omega C_{coupl} + C_{ox}))$ at $R_s = \infty$. Next, we consider the complex reflection coefficient at the plane corresponding to the end of the coaxial geometry at the tip-probe system: Γ_{tip}. The expression for Γ_{tip} in terms of the tip-sample system admittance Y_{tip} is as follows:

$$\Gamma_{tip} = \frac{Y_o - Y_{tip}}{Y_o + Y_{tip}} = \frac{1-\gamma}{1+\gamma} = \frac{2}{1+\gamma} - 1, \quad (1)$$

Equation (1) defines a composite conformal mapping $\gamma \rightarrow \Gamma_{tip}$ consisting of: (a) reciprocation, which is inversion[42] in respect to the unity circle with the center at $\gamma = (-1, 0)$ combined with reflection across the real axis, (b) stretching of the image plane by a factor of two, and (c) a shift by a unit vector in the negative direction along the real axis in the Γ-plane. Importantly, in accordance with properties of the reciprocation, every circle in the γ-plane is mapped onto a circle in the Γ-plane. The right panel of Figure 7b shows a Γ-plane image Γ_{tip} for the R_s-plot in the left panel. This is a circular arc.

The fact of the R_s-semicircle shape conservation under mapping from the Y-plane onto Γ-plane, significantly simplifies interpretation of the image contrast. This becomes more evident if one considers the relation between Y_{tip} and the experimentally measured reflection coefficient at the VNA port Γ_{port}. The measured Γ_{port} can be viewed as a result of a transformation of the reflection coefficient at the tip-sample system Γ_{tip} by the element of the microwave path between the VNA port and the tip-sample system. The effect of the $\lambda/2$ impedance transformer with the shunt resistor combined with the feed cable is equivalent to a shift of R_s-semicircle to the very vicinity of the origin in the Γ-plane with a change of its radius, which can be visualized graphically using standard operations with the Smith chart. It immediately follows, that bringing semicircle to the center of the Γ-plane will result in increased microscope sensitivity in the phase channel, which is observed in the experiments as was mentioned above. In an uncalibrated, imaging system, the position of the R_s arc in the Γ-plane at a fixed frequency can be arbitrary, which leads to a not well-defined contrast behavior in the amplitude and phase images as noticed during imaging of graphene. Both signals can be double-valued functions of the sheet resistance. This fact calls for development of procedures for microscope tuning and calibration based on the ideas of the outlined graphical technique, which is a subject of current and future work.

5. Outlook: In Situ Near-Field Microwave Microscopy

Driven by the call for development of the technique required for in-depth research of energy storage related materials, recently, we have made preliminary investigation of possible advantages of SMM application for in situ imaging of electrical properties of electrode-electrolyte interfaces. An alternative and readily available technique, in situ conductive AFM,[43–45] suffers from two crucial drawbacks, namely: (a) there is a need to establish conductive current path to a bottom current collector, and (b) no meaningful imaging of electronic conduction is possible in a highly conducting liquid environment. The former limitation implies that total resistance of all elements in the tip-electrode system (tip-surface contact, grains of the electrode material, grain boundaries, interface with current collector) are probed and cannot be separated. At the same time, in conductive liquids, the non-local ionic and residual electronic currents to the main body of the tip and cantilever will dominate the signal, precluding measurement of currents from tip-surface junction that contain spatially-resolved information.

Obviating the need for dedicated counter-electrodes due the use of capacitive probe-sample coupling, SMM would be of advantage as an alternative to c-AFM for in situ imaging in electrolytes. On the other hand, with respect to applications in a conducting liquid, use of frequencies above 1 GHz allows a significant reduction (up to elimination) of the influence of the electrolyte conductivity. The parameter, which describes relative contribution of dielectric and conductive properties in an ac response of a media is its loss tangent given by $\tan\delta = \frac{\sigma}{\omega\varepsilon_0\varepsilon}$, where σ and ε is the media conductivity and relative dielectric constant, respectively, ω is angular frequency, and ε_0 is the dielectric constant of vacuum. At $\tan\delta < 1$, displacement currents are larger, than charge transport currents, and capacitive (dielectric) response dominated the resistive one. In such a situation, electrolyte conductivity does not significantly influence, for example, spatial resolution of an electrical probe.[46] At a fixed conductivity, the loss tangent becomes smaller with increasing probing frequency. For an electrolyte with a conductivity $\sigma = 1$ S/m and $\varepsilon = 10$, the loss tangent becomes unity at a frequency of ≈2 GHz. It should be emphasized that it is precisely the use of microwave frequencies that allowed Hasted et al.[47] to measure the subtle effects of ions on the dielectric constant of concentrated aqueous electrolytes back in 1947, the results, which are still of a considerable value nowadays.

The possibility of microwave imaging in liquids has been recently demonstrated.[48,49] To further access the feasibility of using SMM for in situ imaging in electrolytes, we performed extensive full-wave numerical modeling, and **Figure 8** displays the electric field distribution near an SMM probe immersed in an electrolyte with parameters corresponding to sea water. The singular character of the field enhancement at the probe tip apex of the electric field distribution, as required for imaging, is evident in the plot. The result unambiguously shows that SMM at frequencies of a few GHz can be implemented for mapping of electrode/electrolyte interface properties. In particular, in the simplest case, the SMM could be straightforwardly applied for in situ investigations of electronic transport phenomena at the electrode/electrolyte interfaces in energy-storage-related electrochemical systems. The work on development of in situ capability for SMM is planned for the near future.

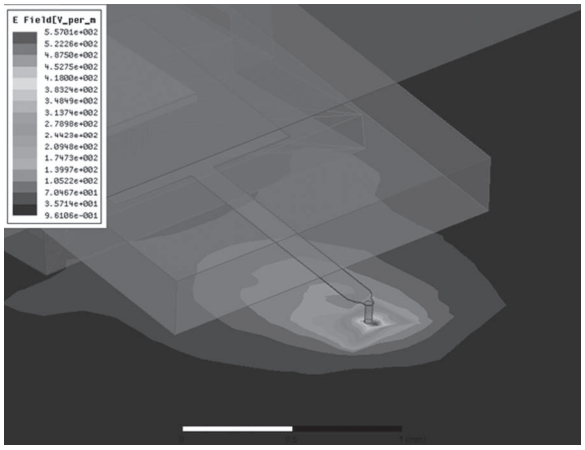

Figure 8. Full-wave (HFSS, Ansoft, Inc.) simulation of electric field amplitude around the SMM probe in a Si sample. The sample and SMM probe are immersed into a dielectric with a dielectric constant $\varepsilon = 80$ and specific conductivity $\sigma = 4$ S/m; frequency is 4 GHz. Scale bar is 0.5 mm.

6. Summary

We have reviewed our recent work on near-field microwave imaging of a metal-insulator transition in a strongly-correlated electron oxide VO_2 and of conductance inhomogeneities in highly technologically relevant forms of graphene. The work was performed on an SMM system incorporated in a widely used AFM platform, which allows routine microwave imaging with a sub-100 nm resolution. Variable-temperature imaging of the metal-insulator in single crystalline nanoplatelets of VO_2 demonstrated a non-trivial strain- and twinning-controlled nucleation of metallic phase in insulating matrix, with the phase transition temperature reduced along twin boundaries of a certain type by as much as 12 K in comparison with the bulk transition. Further, using the nanoplatelets, we introduced a novel principle of electro-mechanical actuation based on the coupled MIT and structural transformation. Images of CVD graphene demonstrated that near-field microwave imaging can be successfully applied to mapping of nanometer-scale defects and associated conductivity inhomogeneities in CVD graphene with a spatial resolution down to 50 nm. We note that this technique can be applied to all optically transparent two-dimensional conductors, when near-field optical imaging is inefficient or impossible. We have also introduced a simple semi-quantitative graphical method guiding interpretation of the contrast in the SMM images, which is especially suited for conducting thin-films. The performed analysis of the contrast formation mechanism in the images of graphene suggests calibration and tuning procedures to open the door to quantitative characterization of the sheet resistance with the SMM. An important direction in the development of the technique can be realization of microwave imaging in situ in highly conducting liquid electrolytes, where use of microwave frequencies can significantly reduce and even eliminate interference of ionic conduction of the electrolyte when imaging solid-electrolyte interfaces.

Acknowledgements

This research was conducted at the Center for Nanophase Materials Sciences, which is sponsored at Oak Ridge National Laboratory by the Scientific User Facilities Division, Office of Basic Energy Sciences, U.S. Department of Energy.

Received: November 21, 2012
Revised: February 14, 2013
Published online: April 2, 2013

[1] B. T. Rosner, D. W. van der Weide, *Rev. Sci. Instrum.* **2002**, *73*, 2505.
[2] S. M. Anlage, V. V. Talanov, A. R. Schwartz, in *Scanning Probe Microscopy: Electrical and Electromechanical Phenomena at the Nanoscale* (Eds: S. V. Kalinin, A. Gruverman), Springer Scientific, New York **2007**, p. 215.
[3] C. A. Paulson, D. W. van der Weide, in *Scanning Probe Microscopy: Electrical and Electromechanical Phenomena at the Nanoscale* (Eds: S. V. Kalinin, A. Gruverman), Springer Scientific, New York **2007**, p. 315.
[4] M. Fee, S. Chu, T. W. Hänsch, *Opt. Commun.* **1989**, *69*, 219.
[5] C. Gao, X. D. Xiang, *Rev. Sci. Instrum.* **1998**, *69*, 3846.
[6] S.-C. Lee, C. P. Vlahacos, B. J. Feenstra, A. Schwartz, D. E. Steinhauer, F. C. Wellstood, S. M. Anlage, *Appl. Phys. Lett.* **2000**, *77*, 4404.
[7] D. E. Steinhauer, C. P. Vlahacos, S. K. Dutta, B. J. Feenstra, F. C. Wellstood, S. M. Anlage, *Appl. Phys. Lett.* **1998**, *72*, 861.
[8] V. V. Talanov, A. Scherz, R. L. Moreland, A. R. Schwartz, *Appl. Phys. Lett.* **2006**, *88*, 134106.
[9] V. V. Talanov, C. D. Barga, L. Wickey, I. Kalichava, E. Gonzales, E. A. Shaner, A. V. Gin, N. G. Kalugin, *ACS Nano* **2010**, *4*, 3831.
[10] K. Lai, W. Kundhikanjana, M. Kelly, Z.-X. Shen, *Rev. Sci. Instrum.* **2008**, *79*, 063703.
[11] H. P. Huber, M. Moertelmaier, T. M. Wallis, C. J. Chiang, M. Hochleitner, A. Imtiaz, Y. J. Oh, K. Schilcher, M. Dieudonne, J. Smoliner, P. Hinterdorfer, S. J. Rosner, H. Tanbakuchi, P. Kabos, F. Kienberger, *Rev. Sci. Instrum.* **2010**, *81*, 113701.
[12] M. Tabib-Azar, D. P. Su, A. Pohar, S. R. LeClair, G. Ponchak, *Rev. Sci. Instrum.* **1999**, *70*, 1725.
[13] M. Abu-Teir, M. Golosovsky, D. Davidov, A. Frenkel, H. Goldberger, *Rev. Sci. Instrum.* **2001**, *72*, 2073.
[14] J. Kim, K. Lee, B. Friedman, D. Cha, *Appl. Phys. Lett.* **2003**, *83*, 1032.
[15] G. Chen, B. Hu, I. Takeuchi, K.-S. Chang, X.-D. Xiang, G. Wang, *Meas. Sci. Technol.* **2005**, *16*, 248.
[16] Q. Zhang, P. J. McGinn, *J. Am. Ceram. Soc.* **2006**, *89*, 1687.
[17] A. Imtiaz, S. M. Anlage, J. D. Barry, J. Melngailis, *Appl. Phys. Lett.* **2007**, *90*, 143106.
[18] K. Lai, M. Nakamura, W. Kundhikanjana, M. Kawasaki, Y. Tokura, M. A. Kelly, Z.-X. Shen, *Science* **2010**, *329*, 190.
[19] J. Lee, C. J. Long, H. Yang, X.-D. Xiang, I. Takeuchi, *Appl. Phys. Lett.* **2010**, *97*, 183111.
[20] A. Tselev, V. Meunier, E. Strelcov, W. A. Shelton, I. A. Luk'yanchuk, K. Jones, R. Proksch, A. Kolmakov, S. V. Kalinin, *ACS Nano* **2010**, *4*, 4412.
[21] A. Tselev, S. M. Anlage, Z. Ma, J. Melngailis, *Rev. Sci. Instrum.* **2007**, *78*, 044701.
[22] M. Farina, A. Lucesoli, T. Pietrangelo, A. di Donato, S. Fabiani, G. Venanzoni, D. Mencarelli, T. Rozzi, A. Morini, *Nanoscale* **2011**, *3*, 3589.
[23] A. Imtiaz, S. M. Anlage, *Ultramicroscopy* **2003**, *94*, 209.
[24] M. S. Kim, S. Kim, J. Kim, K. Lee, B. Friedman, J.-T. Kim, J. Lee, *Rev. Sci. Instrum.* **2003**, *74*, 3675.
[25] D. W. van der Weide, P. Neuzil, *J. Vac. Sci. Technol., B* **1996**, *14*, 4144.

[26] M. Tabib-Azar, Y. Wang, *IEEE Trans. Microw. Theory Technol.* **2004**, *52*, 971.
[27] Y. Wang, A. D. Bettermann, D. W. van der Weide, *J. Vac. Sci. Technol., B* **2007**, *25*, 813.
[28] K. Lai, M. B. Ji, N. Leindecker, M. A. Kelly, Z.-X. Shen, *Rev. Sci. Instrum.* **2007**, *78*, 063702.
[29] A. Karbassi, D. Ruf, A. D. Bettermann, C. A. Paulson, D. W. van der Weide, H. Tanbakuchi, R. Stancliff, *Rev. Sci. Instrum.* **2008**, *79*, 094706.
[30] A. Tselev, E. Strelcov, I. A. Luk'yanchuk, J. D. Budai, J. Z. Tischler, I. N. Ivanov, K. Jones, R. Proksch, S. V. Kalinin, A. Kolmakov, *Nano Lett.* **2010**, *10*, 2003.
[31] L. Zhang, Y. Ju, A. Hosoi, A. Fujimoto, *Rev. Sci. Instrum.* **2010**, *81*, 123708.
[32] W. Kundhikanjana, K. Lai, H. Wang, H. Dai, M. A. Kelly, Z.-X. Shen, *Nano Lett.* **2009**, *9*, 3762.
[33] K. Lai, H. Peng, W. Kundhikanjana, D. T. Schoen, C. Xie, S. Meister, Y. Cui, M. A. Kelly, Z.-X. Shen, *Nano Lett.* **2009**, *9*, 1265.
[34] S. Wu, J.-J. Yu, *Appl. Phys. Lett.* **2010**, *97*, 202902.
[35] C. Plassard, E. Bourillot, J. Rossignol, Y. Lacroute, E. Lepleux, L. Pacheco, E. Lesniewska, *Phys. Rev. B* **2011**, *83*, 121409.
[36] Y. Cho, S. Kazuta, K. Matsuura, *Appl. Phys. Lett.* **1999**, *75*, 2833.
[37] K. Tanaka, Y. Kurihashi, T. Uda, Y. Daimon, N. Odagawa, R. Hirose, Y. Hiranaga, Y. Cho, *Jpn. J. Appl. Phys.* **2008**, *47*, 3311.
[38] K. Lai, W. Kundhikanjana, M. A. Kelly, Z.-X. Shen, J. Shabani, M. Shayegan, *Phys. Rev. Lett.* **2011**, *107*, 176809.
[39] A. Tselev, I. A. Luk'yanchuk, I. N. Ivanov, J. D. Budai, J. Z. Tischler, E. Strelcov, A. Kolmakov, S. V. Kalinin, *Nano Lett.* **2010**, *10*, 4409.
[40] A. Tselev, J. D. Budai, E. Strelcov, J. Z. Tischler, A. Kolmakov, S. V. Kalinin, *Nano Lett.* **2011**, *11*, 3065.
[41] A. Tselev, N. V. Lavrik, I. Vlassiouk, D. P. Briggs, M. Rutgers, R. Proksch, S. V. Kalinin, *Nanotechnology* **2012**, *23*, 385706.
[42] E. W. Weisstein, *CRC Concise Encyclopedia of Mathematics*, Chapman & Hall/CRC, Boca Raton **2003**.
[43] R. Kostecki, F. McLarnon, *Electrochem. Solid-State Lett.* **2004**, *7*, A380.
[44] T. M. McEvoy, K. J. Stevenson, *Langmuir* **2005**, *21*, 3521.
[45] D. A. Bussian, J. R. O'Dea, H. Metiu, S. K. Buratto, *Nano Lett.* **2007**, *7*, 227.
[46] N. Balke, A. Tselev, T. M. Arruda, S. Jesse, Y.-H. Chu, S. V. Kalinin, *ACS Nano* **2012**.
[47] J. B. Hasted, D. M. Ritson, C. H. Collie, *J. Chem. Phys.* **1948**, *16*, 1.
[48] N. Kobayashi, H. Asakawa, T. Fukuma, *Rev. Sci. Instrum.* **2010**, *81*, 123705.
[49] M. Farina, A. Di Donato, D. Mencarelli, G. Venanzoni, A. Morini, *IEEE Microwave and Wireless Components Letters* **2012**, *22*, 595.